Surface charge induced ferroelectric semiconductor-to-metal transition in quintuple-layer Al_2S_3

Xinli Wang,[1,2] Juping Xu,[1,2] Peng-Fei Liu,[1,2] Bao-Tian Wang,[1,2] and Wen Yin[1,2,3,*]

[1]*Institute of High Energy Physics, Chinese Academy of Sciences (CAS), Beijing 100049, People's Republic of China*

[2]*Spallation Neutron Source Science Center, Dongguan 523803, People's Republic of China*

[3]*University of Chinese Academy of Sciences, Beijing 100049, People's Republic of China*

(Received 22 November 2022; revised 14 June 2023; accepted 15 June 2023; published 29 June 2023)

For two-dimensional (2D) polarized monolayers or type-II heterostructure semiconductors, the semiconductor-to-metal transition (SMT) process usually occurs under doping engineering or external electric field. In this work, we point out that the evolution of band offset, surface charge redistribution, and inner-layer charge transfer are synergetic in polarized monolayer semiconductors. Taking quintuple-layer (QL) Al_2S_3 as an example, the SMT process occurs by substituting the surface S atom with the O atom and applying external electric field by two methods. Our results reveal that the SMT derives from the increased surface charge on two-surface atoms. The SMT mechanism in polarized QL-Al_2S_3 is also applicable to other 2D polarized monolayers and heterostructure semiconductors.

DOI: 10.1103/PhysRevB.107.235307

I. INTRODUCTION

Recently, a family of group III-VI binary monolayers, M_2X_3 (M = Al, Ga, In and X = O, S, Se, Te) consists of five atomic sublayers stacking as X-M-X-M-X are proposed and widely studied. Experimentally, various M_2X_3 systems such as In_2Se_3 [1–3], In_2S_3 [4], and Ga_2S_3 [5,6] have been fabricated. Theoretically, Ding *et al.* [7] reported a family of two-dimensional (2D) intrinsic ferroelectric (FE) compounds M_2X_3 (M = Al, Ga, In and X = S, Se, Te), in which the asymmetric structure and out-of-plane ferroelectric properties suggest these monolayers are promising for photocatalyst water splitting [8,9], ferroelectric tunnel barrier [10,11], data storage devices [12–15], and optoelectronic devices [16–19].

Among these hexagonal III-VI binary monolayers, 2D aluminum monochalcogenide and Janus aluminum chalcogenide monolayers with the chemical formula Al_2X_3 and Al_2XY_2 (X/Y = O, S, Se, and Te) has also been widely researched. Experimentally, 2D quintuple-layer (QL) Al_2O_3 structures comprised of tetrahedral and octahedral coordinated Al-O units have been directly observed on AlN surfaces by aberration corrected scanning transmission electron microscopy (STEM) imaging and spectroscopy [20]. Theoretically, Meng *et al.* [21] have explored the stability, crystal structure, mechanical, electronic, and optical properties of three kinds of Al_2O_3 monolayers. Jin *et al.* [22] have found that QL Al_2O_3 can be as a functional ferroelectric tunnel barrier in a graphene/QL-Al_2O_3/Ru heterostructure. Tuan *et al.* [23] investigated the electronic and transport properties of Janus Al_2XY_2 (X/Y = S, Se, Te; $X \neq Y$) monolayers. They demonstrated that all Al_2XY_2 monolayers exhibit high electron mobility, suggesting that they are suitable for applications in nanometer-sized electronic devices.

The semiconductor-to-metal transition (SMT) in 2D monolayer or heterostructure semiconductors are usually achieved by doping or applying external electric field (E_{ext}) [24–30]. The SMT phenomenon is also common in the group of M_2X_3 monolayer. The substitution of aliovalent As for Se in α-In_2Se_3 transforms it from a nonmagnetic semiconductor to a metal with ferromagnetism [31]. A similar situation is reported in 2D X_2NO_2 (X = In, Tl) monolayers with O substituted by an N atom [32]. In addition, QL Ga_2S_3 [8] and QL Ga_2O_3 [33] are indirect-band-gap semiconductors while the Janus QL Ga_2SO_2 is metallic [34]. Similarly, QL Al_2TeS_2 [23] and QL In_2TeS_2 [35] are also metals, which are different from QL Al_2S_3 and QL In_2S_3 [8] with indirect band gaps. Coincidentally, in another III-VI binary compound, MX (M = B, Al, Ga, In, and X = O, S, Se, Te) monolayers, the SMT by constructing Janus M_2XY (X/Y = O, S, Se, and Te) configurations has also been reported [36–41]. Compared with M_2X_3 (MX) monolayers, Janus M_2XY_2 (M_2XY) monolayers possess a built-in electric field due to the electronegativity difference of the group-VI element [38,39]. Meanwhile, the SMT also comes out by directly applying a perpendicular external electric field (E_{ext}) to InSe and In_2Se_3 monolayers [42]. The fundamental reason for the evolution of band structures with electric field (external or intrinsic polarization) in polarized monolayer semiconductors is unclear.

For 2D type-II heterostructure semiconductors, the SMT occurs under E_{ext} with the band gap depending on the strength and the direction of the E_{ext} [43–51]. Interestingly, the band gap decreases directly with increasing E_{ext} along one direction, while the band gap increases first and then decreases with increasing E_{ext} along the opposite direction [49–51]. The changes of band gap under the increasing negative direction and positive direction E_{ext} are different. Previous researches have reported that not only do the band gaps but interface charge transfer also change under E_{ext} in 2D type-II heterostructures. So, we assume that the evolution of band

*yinwen@ihep.ac.cn

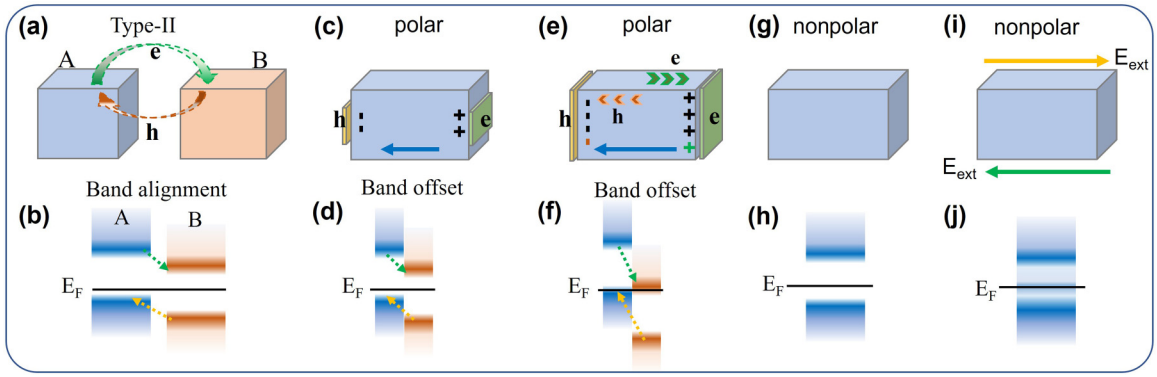

FIG. 1. (a), (b) The schematic diagram of interface charge transfer and energy transfer in 2D type-II semiconductor heterostructures. (c), (e) The schematic diagrams of spatially separated charge distribution on the surfaces of polarized monolayer. The positive and negative polarization (bound) charge center are labeled by "+" and "−" in the two surfaces. The blue arrow indicates the direction of the intrinsic polarization electric field. The hole and electron are shown with thin yellow and green slab on the two surfaces. The higher yellow and green slab in (e) compared with in (c) represent the increased hole and electron on two surfaces. (d), (f) The band offsets of polarized monolayer correspond to (c) and (e). The nonpolar monolayer semiconductor and corresponding band structure without (g), (h) and with (i), (j) E_{ext}.

alignment is related to the surface charge redistribution in type-II heterostructures. The basis of this assumption is that the shifting energy level and changing surface charge can be connected through interface charge transfer. The unidirectional interface charge transfer results in being more electron (hole) and down (up) shifting conduction (valence) band in the *B* (*A*) layer, as shown in Figs. 1(a) and 1(b). The separated charge distribution is present in 2D polarized monolayers in Figs. 1(c) and 1(e). We wonder whether the shifting energy level in monolayers comes from the increased surface charge induced by inner-layer charge transfer driven by increased polarization electric field or E_{ext} in 2D polar monolayer or nonpolar monolayer semiconductors, as shown in Figs. 1(e) and 1(f), and 1(i) and 1(j).

In this work, we propose that increased surface charge induces the SMT in polarized monolayers. The premise for this SMT mechanism is the spatial separated electron and hole, which is one common phenomenon in 2D polarized monolayers and type-II heterostructure semiconductors. Choosing QL Al_2S_3 as a model system, we reveal the native SMT mechanism by the O substituted method (experimentally feasible [52–54]) and applying the E_{ext} method. The SMT originates from the increased surface charge, which is also suitable for other 2D polarized monolayer and heterostructure semiconductor materials.

II. COMPUTATIONAL DETAILS

The atomic structure of QL-Al_2S_3 monolayer in Fig. 2(a) is composed with octahedral coordinated S-Al-S trilayer and tetrahedral coordinated Al-S bilayer [8,20]. In this work, we adopt the ferroelectric wurtzite (FE-WZ′) [22] QL-Al_2S_3 phase, in which the S atoms are stacked in *A*-*B*-*C* sequences and the Al atoms are located at octahedral (Al_{oct}) and tetrahedral (Al_{tet}) interstitial sites of S lattice atoms [55,56].

By substituting one S atom on the tetrahedral termination surface or the octahedral termination surface in the unit cell of QL Al_2S_3, we construct two kinds of Janus QL-$Al_2S_xO_{3-x}$ alloy phases, QL-$Al_2S_2O_{tet}$ and QL-$Al_2S_2O_{oct}$, as shown in Figs. 2(b) and 2(c). The configuration of the substituted O atom on the tetrahedral termination surface is more energetically favorable than the configuration of the substituted O atom on the octahedral termination surface.

The geometric structures, stability, and electronic structures of these monolayers are performed using the VASP (Vienna *ab initio* simulation) software package [57] based on the density functional theory [58]. The projector augmented wave approach [59] was used for describing the interaction of electron and atom core. The exchange correlation potential was the PBE potential in the generalized gradient approximation (GGA) [60]. The electronic structures were calculated using the HSE06 [61] functional with mixing parameter for the Hartree-Fock potential being set to 0.25. The cutoff energy was set as 500 eV. The convergence criteria

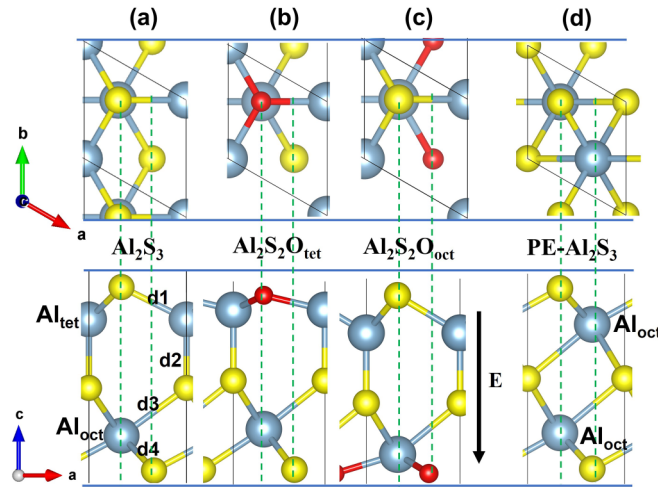

FIG. 2. Top and side view of QL-Al_2S_3 (a), QL-$Al_2S_2O_{tet}$ (b), QL-$Al_2S_2O_{oct}$ (c) configuration. The red, yellow, and blue sphere represents O, S, and Al atoms respectively. These configurations are asymmetric and with out-of-plane polarization. The black arrow indicates the direction of the intrinsic polarization electric field. (d) Top and side view of paraelectric (PE) phase Al_2S_3 configuration with symmetric atomic structure; Al atoms locate at the octahedral interstitial sites of S lattice atoms.

TABLE I. The calculated lattice constant (a), bond length (d), thickness of the QL-Al_2S_3 and O-substituted QL-Al_2S_3 monolayer.

QL	$a = b$ (Å)	[[Al_{tet}S(O)]] (Å) $d1$	$d2$	d[Al_{oct} S(O)] (Å) $d3$	$d4$	Thickness (Å)
Al_2S_3	3.586	2.312	2.183	2.570	2.348	5.843
$Al_2S_2O_{tet}$	3.313	1.968	2.206	2.446	2.288	5.449
$Al_2S_2O_{oct}$	3.336	2.245	2.164	2.501	2.014	5.503

for the Hellmann-Feynman force and energy were less than 0.001eV $Å^{-1}$ and 10^{-5} eV, respectively. The 5×5×1 Γ−centered k-point mesh was used for the geometry relaxations and 10×10×1 Γ−centered k-point mesh was used for electronic property calculations.

A vacuum layer of 15 Å was applied to cancel the interaction between layers. The dipole correction is included in the calculations. The charge transfer between atoms is evaluated on the basis of the Bader charge algorithm [62]. Phonon spectra were calculated on the basis of density functional perturbation theory method by using the PHONOPY program [63]. The thermodynamic stability of free-standing QL-Al_2S_3 and $Al_2S(O)_3$ structures was judged based on Ab Initio Molecular Dynamic (AIMD) simulations [64]. The simulations lasted for 10 ps in the canonical ensemble controlled by a Nose-Hoover thermostat (*NVT*) [65] with a time step of 2 fs at 300 K. The electronic properties were analyzed with the VASPKIT [66] package. The atomic configurations and charge density difference were visualized by the VESTA [67] package.

III. RESULTS

A. Geometry and stability

After structural relaxation, the optimized lattice parameters and bond lengths of QL Al_2S_3 and O-substituted QL Al_2S_3 monolayers are tabulated in Table I. The lattice parameter of QL-Al_2S_3 monolayer is 3.586 Å, which consist with the previous theoretical values [8]. Structurally, the bond length between Al-O ($d_{Al\text{-}O}$) is shorter than that of Al-S ($d_{Al\text{-}S}$) bond. The thickness of an O-substituted QL-Al_2S_3 system becomes thinner than that of QL-Al_2S_3 with more Al-O bonds. The bond length of Al-O being shorter than Al-S corresponds to the binding energy of Al-O being stronger than Al-S, which originates from the electronegativity of O atoms being higher than S atoms [38,39]. The electronegativity difference ($\Delta\chi$) and charge transfer ($\Delta\rho$) between the Al-O atom pair are larger than those of the Al-S atom pair [38,39].

Figure 3(a) shows the phonon band structure and corresponding phonon density of states (PHDOS) of QL Al_2S_3. Since no negative frequency phonon can be observed, the QL-Al_2S_3 monolayer is dynamically stable. After 10 ps simulation, no distinct structural destruction is observed in Fig. 3(b), and the total energy fluctuation is small. This finding indicates that the QL-Al_2S_3 monolayer is thermally stable at 300 K. For QL-$Al_2S_2O_{tet}$ and QL-$Al_2S_2O_{oct}$ configurations, the phonon band structures and corresponding PHDOS of S, O, and Al atoms are shown in Figs. S1(a) and S1(b) of the Supplemental Material [68]. Although no negative frequency phonon can be observed, the AIMD results [Figs. S2(a)–S2(d) of the Supplemental Material [68]] reveal that these structures deform at 300 K, indicating that they are thermodynamically unstable at elevated temperature. That is because the shorter Al-O bond on the QL-Al_2S_3 surface will break and the broken Al-O bonds will reconstruct to form Al-O clusters.

B. Band structure variation with different O atoms substituted

The band structures of three configurations shown in Figs. 2(a)–2(c) evaluated by the PBE and HSE06 approaches are almost the same profile, as shown in Figs. 4(a)–4(c). These monolayers are nonmagnetic materials. It is interesting to find that the QL-Al_2S_3 and QL-$Al_2S_2O_{oct}$ monolayers are indirect band-gap semiconductors, while the QL-$Al_2S_2O_{tet}$ monolayer is metal. The conduction band minimum (CBM) and valence

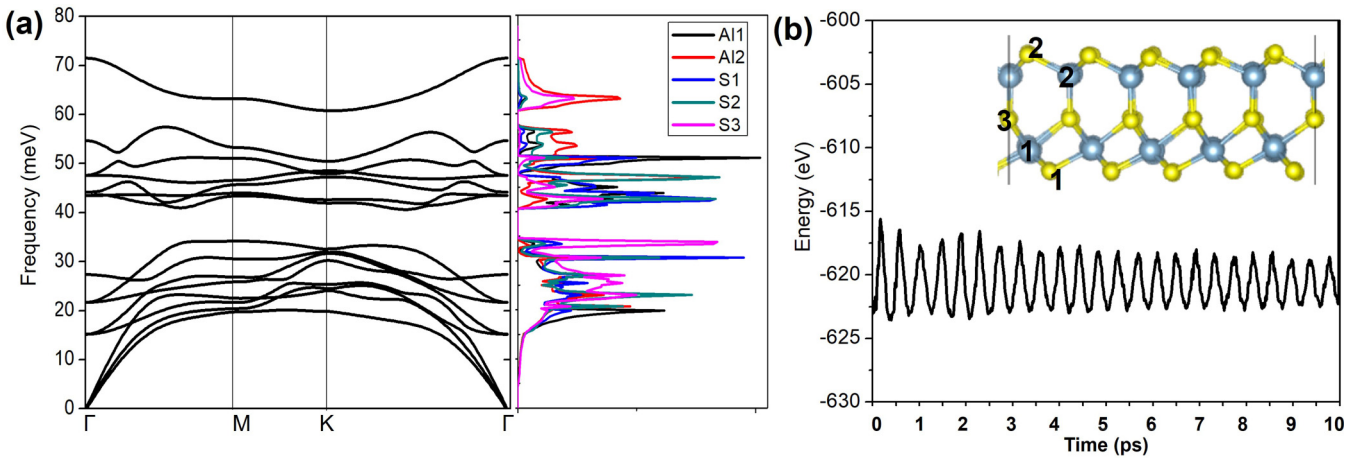

FIG. 3. (a) The phonon spectra and corresponding PHDOS of QL-Al_2S_3 monolayer. (b) The AIMD simulations of QL-Al_2S_3 monolayer. The inset is the relaxed atomic structure of QL-Al_2S_3 monolayer after 10 ps.

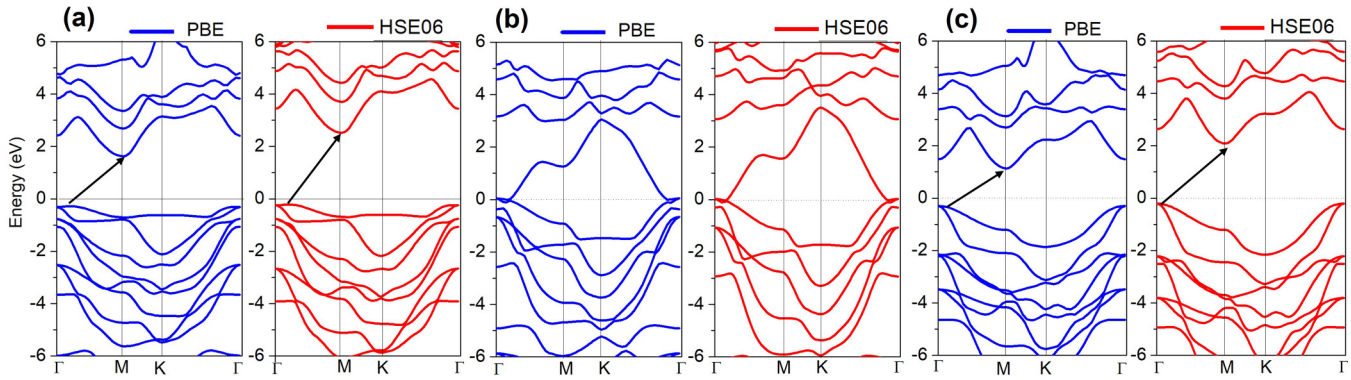

FIG. 4. Band structure of QL-Al_2S_3 (a), QL-$Al_2S_2O_{tet}$ (b), and QL-$Al_2S_2O_{oct}$ (c) monolayers at the PBE (blue curves) and HSE06 (red curves) levels. The Fermi level is set to zero and depicted by the gray line.

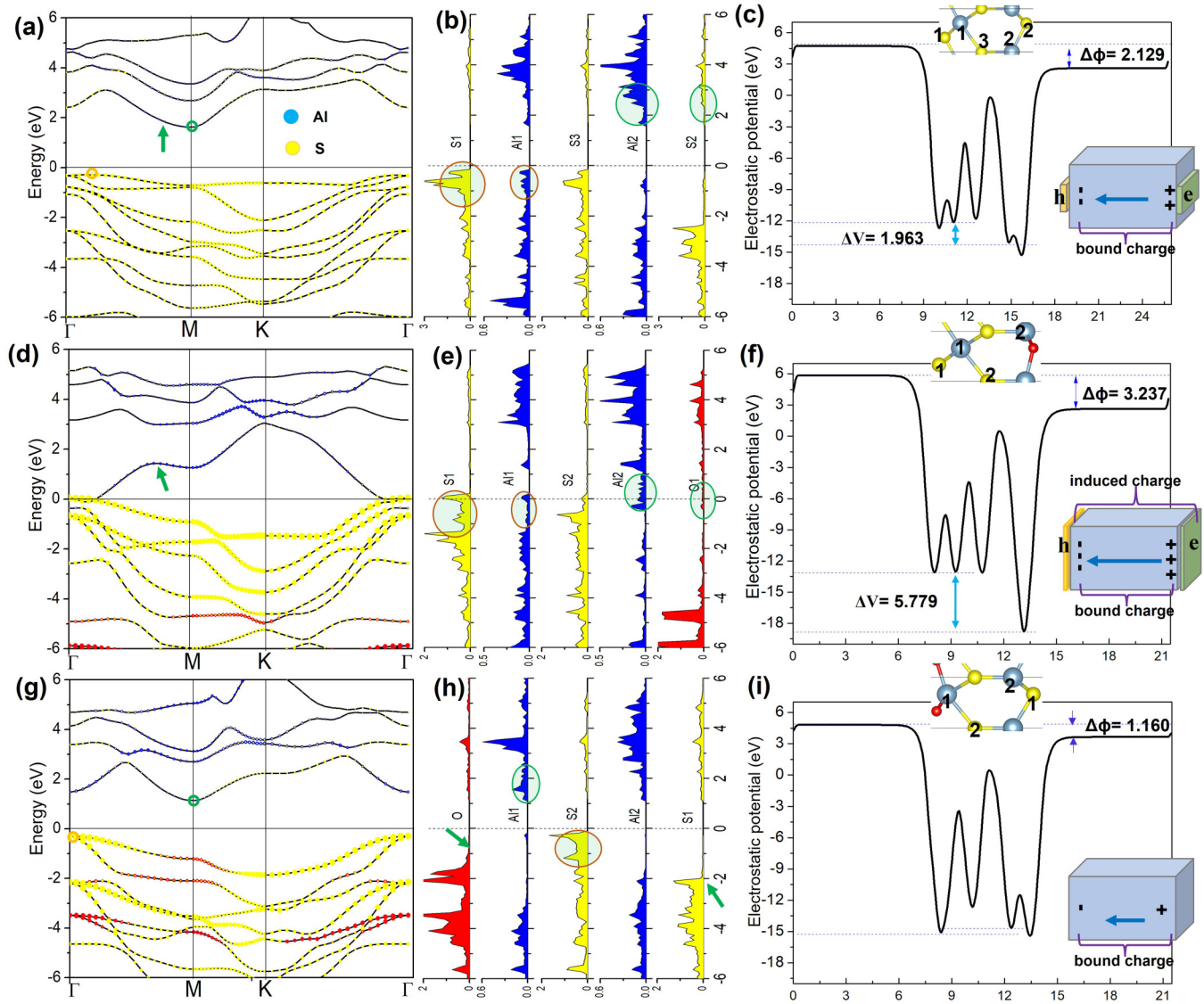

FIG. 5. (a), (b) Band structure and the layer-resolved PDOS of QL Al_2S_3. The Fermi level is set to zero. The blue, yellow, and red color coding represent the contribution weights from Al, S, and O atoms, respectively. (c) The planar-averaged electrostatic potential for QL Al_2S_3 along the z axis. $\Delta\phi$ depict the potential difference across the monolayer. The corresponding electronic properties of QL-$Al_2S_2O_{tet}$ (d)–(f) and QL-$Al_2S_2O_{oct}$ (g)–(i) monolayer. The blue arrow indicates the direction of the intrinsic polarization electric field.

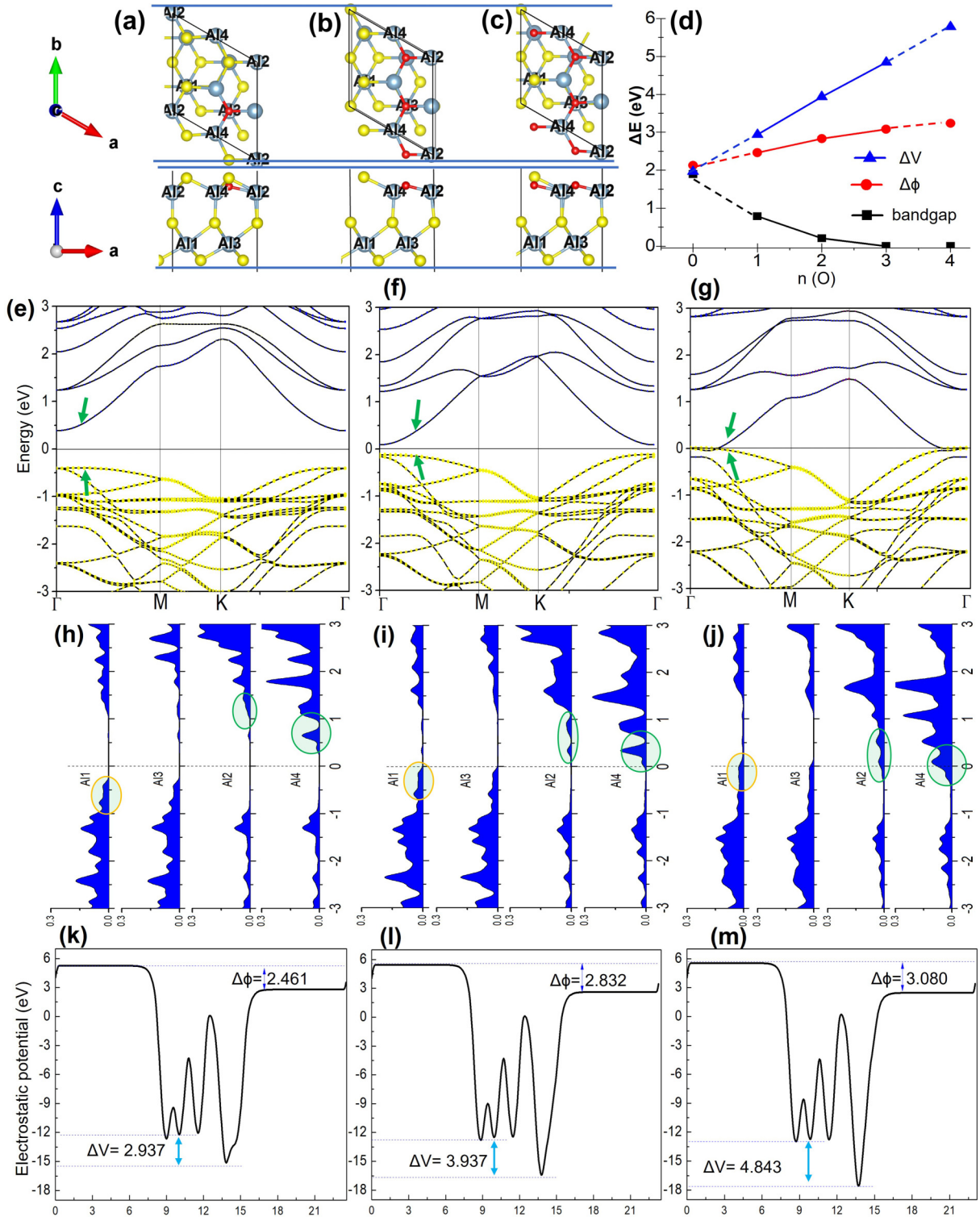

FIG. 6. Side and top views of (2×2) supercell QL-Al_2S_3 monolayer with different substituted O atoms on tetrahedral termination surface (a)–(c). The band gap, ΔV, and $\Delta\phi$ as functions of the number of O atoms are summarized in (d). (e)–(g) The band structures of (2×2) QL Al_2S_3 with surface O atoms from 1 to 3. (h)–(j) The layer-resolved PDOS of Al atoms along the z axis. All Fermi energy levels are shifted to zero. (k)–(m) The planar-averaged electrostatic potential for O-doped QL Al_2S_3 along the z axis.

band maximum (VBM) of QL-Al_2S_3 and QL-$Al_2S_2O_{oct}$ monolayers are located at the M point and near the Γ point along Γ-M in the Brillouin zone, respectively. The band gaps of QL-Al_2S_3 and QL-$Al_2S_2O_{oct}$ monolayers are 1.90 (2.74) and 1.407 (2.295) eV at the PBE (HSE06) level, respectively. Our calculated result for the band gap of QL-Al_2S_3 is comparable with the previous DFT calculations [8].

Next, the detailed electric properties of three monolayers are analyzed based on the PBE level. The valence bands of QL-Al_2S_3 are mainly contributed by the S atoms while the Al

TABLE II. Bader charges of QL-Al_2S_3, QL-$Al_2S_2O_{tet}$, and QL-$Al_2S_2O_{oct}$ monolayers. Positive and negative values represent the electron depletion and accumulation.

Bader	S(O)	Al_{oct}	S(O)	Al_{tet}	S(O)
QL Al_2S_3	−1.392	+2.197	−1.493	+2.179	−1.491
QL $Al_2S_2O_{tet}$	−1.340	+2.243	−1.524	+2.312	−1.691
QL $Al_2S_2O_{oct}$	−1.574	+2.364	−1.485	+2.190	−1.495

atoms dominate the conduction bands in Fig. 5(a). Different from the band structure of QL Al_2S_3, the lowest conduction band and highest valence band in the band structure of QL $Al_2S_2O_{tet}$ pass through the Fermi level (E_F) in Fig. 5(d). In the layer-resolved projected density of states (PDOS) of these two configurations, it is worth noting that all the conduction band minimum (CBM) is from the Al_{tet}-S(O) bilayer on tetrahedral surface termination and all the valence band maximum (VBM) is from the S-Al_{oct}-S trilayer on octahedral surface termination.

Compared with QL Al_2S_3, the layer-resolved PDOS clearly shows that the metallicity in QL $Al_2S_2O_{tet}$ originates from the shifted CBM (down) and VBM (up), which come from two separated surfaces. As we know, doping in the semiconductor affects the Fermi level. It is important to assume that the shifted VBM and CBM to E_F represent the increased surface charge (hole and electron) on two surfaces. It is worth noting that there are two sets of spatially separated surface charge in the FE QL Al_2S_3: One is the intrinsic polarization charge and the other is the induced (free) charge. In

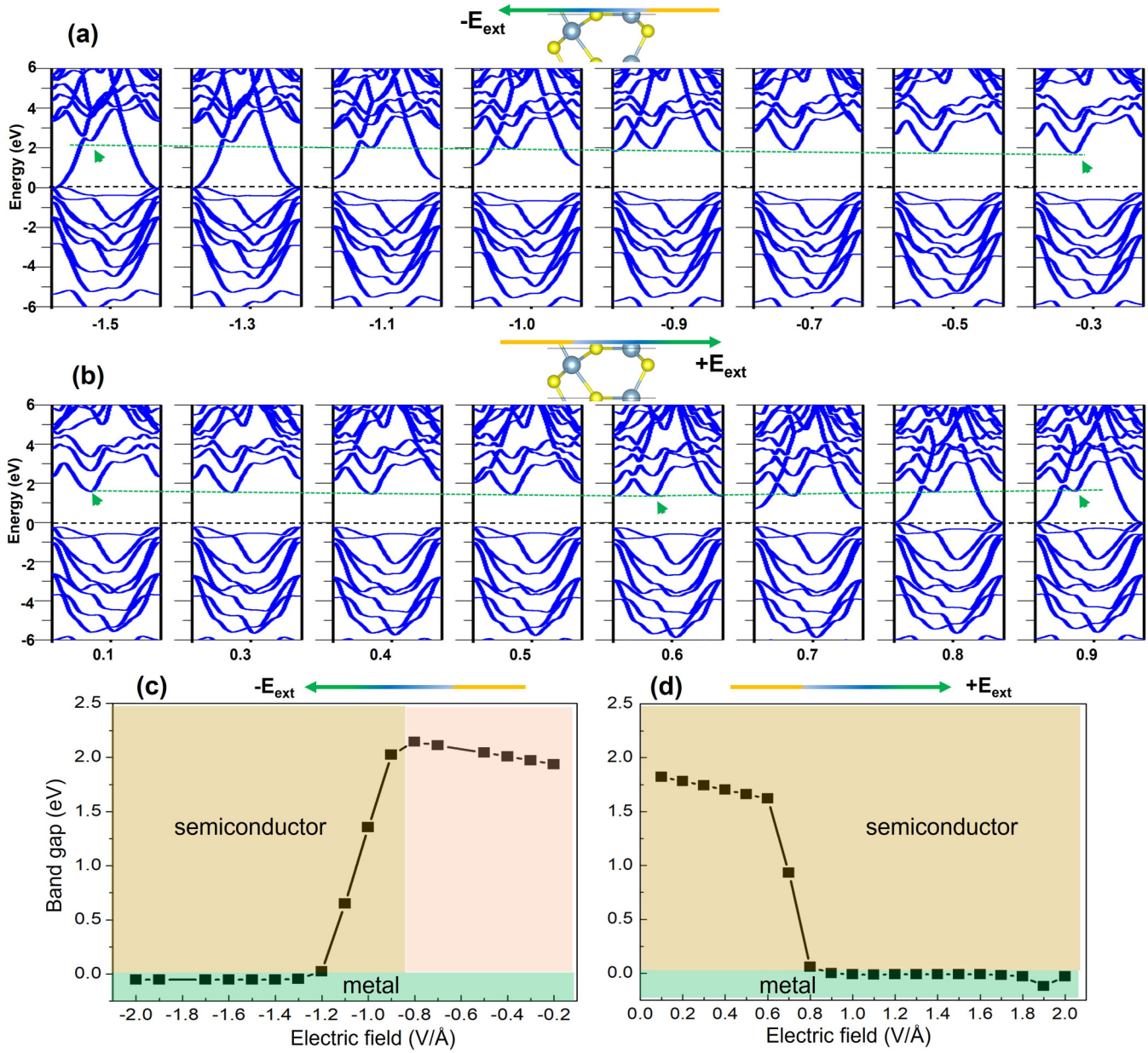

FIG. 7. Evolution of the band structure of QL Al_2S_3 under the different external electric fields points to the negative direction (a) and positive direction (b). (c), (d) The band gap evolution of QL Al_2S_3 under the different external electric fields.

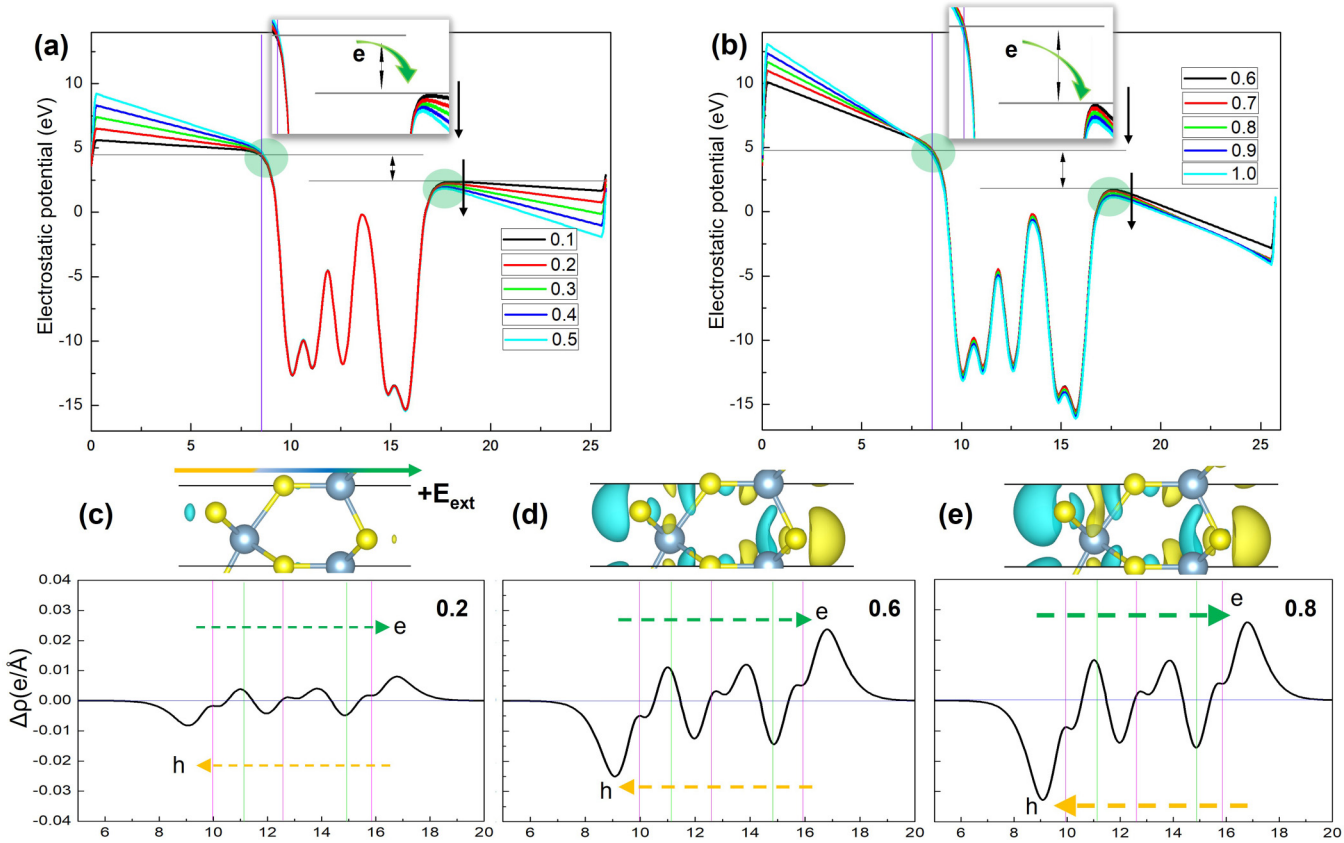

FIG. 8. (a), (b) The planar-averaged electrostatic potential distribution as a function of positive E_{ext} in QL Al_2S_3. (c)–(e) The charge density difference of QL Al_2S_3 under positive (0.2, 0.6, 0.8 V/Å) electric field. The blue and yellow regions represent electron depletion and accumulation respectively. The isosurface values are set at 0.0003 e/Å.

addition, the induced (free) charge, electron and hole, always accompanies the polarization (positive and negative) charge in FE materials [69,70]. The number of polarization charge is positively correlated with the total electrostatic potential difference ($\Delta\phi$) in 2D ferroelectric materials [56,71]. Next, we will focus on the distribution of electrostatic potential and the $\Delta\phi$ across these polarized monolayers.

The electrostatic potential of Al_{oct} termination is higher than that of Al_{tet} termination by 2.129 eV in QL Al_2S_3 in Fig. 5(c). It is necessary to point out that the Al_{oct} termination with higher potential is equivalent to the center of negative polarization (bound) charge. By contrast, the Al_{tet} termination with lower potential is equivalent to the center of positive polarization (bound) charge. The electrostatic potential of Al_{oct} termination is higher than that of Al_{tet} termination by 3.237 and 1.160 eV in QL $Al_2S_2O_{tet}$ and QL-$Al_2S_2O_{oct}$ in Figs. 5(f) and 5(i).

It is worth noting that the larger $\Delta\phi$ derives from the decreased potential of the Al_{tet} atom in QL $Al_2S_2O_{tet}$ than that in QL-Al_2S_3, which is due to the stronger electronegativity of the O atom than of the S atom [38,39]. The larger $\Delta\phi$ in QL $Al_2S_2O_{tet}$ than in QL Al_2S_3 means more polarization charge on surfaces. In contrast, the decreased $\Delta\phi$ in QL $Al_2S_2O_{oct}$ than in QL Al_2S_3 is due to the decreased potential of Al_{oct} atom termination. Different from type-II heterostructures, in which the shifting of CBM and VBM originates from the interface charge transfer between two layers, in monolayer the shifting is from the inner-layer charge transfer [72]. It is interesting to find that the internal potential difference (ΔV) between the Al_{oct} and Al_{tet} atoms becomes larger in QL $Al_2S_2O_{tet}$ than in QL-Al_2S_3 in Figs. 5(c) and 5(f). In contrast, the internal potential difference (ΔV) between the Al_{oct} and Al_{tet} atoms decreases to zero in QL $Al_2S_2O_{oct}$ in Figs. 5(c) and 5(i). The increased $\Delta\phi$ and ΔV of QL $Al_2S_2O_{tet}$ than in QL-Al_2S_3 correspond to more charge transfer toward the Al_{tet} termination. The decreased $\Delta\phi$ and ΔV of QL $Al_2S_2O_{oct}$ than in QL Al_2S_3 correspond to fewer charge transfer toward the Al_{tet} termination or increased charge transfer toward the Al_{oct} termination inside monolayers.

From the Bader charge analysis (see Table II), we can clearly see the increased surface charge of the O atom on tetrahedral termination and the decreased surface charge of the S atom on octahedral termination in QL $Al_2S_2O_{tet}$. The charge of Al_{oct} and Al_{tet} atoms in QL $Al_2S_2O_{tet}$ is larger than in QL Al_2S_3. In addition, the effective charge value and charge increment of Al_{tet} are larger than that of Al_{oct}, meaning more electron transfer from Al_{tet} to surface O atoms, which is consistent with the lower potential of Al_{tet} atoms. On the contrary, the increased surface charge of the O atom on octahedral termination and the charge of Al_{oct} mean more transferred electrons from Al_{oct} to surface O atoms in QL-$Al_2S_2O_{oct}$.

The variable band structures of oxidized QL Al_2S_3 depend on the change of surface charge (electron and hole) on two surface atoms. To further verify this point, by changing the

TABLE III. Bader charges of QL-Al_2S_3 monolayer under negative and positive direction E_{ext}. Positive and negative values represent the electron depletion and accumulation.

E_{ext} (V/Å)	S	Al_{oct}	S	Al_{tet}	S
−1.2	−1.442	+2.199	−1.489	+2.183	−1.451
−0.8	−1.424	+2.199	−1.493	+2.182	−1.464
−0.3	−1.406	+2.198	−1.493	+2.273	−1.482
0.0	−1.392	+2.197	−1.493	+2.179	−1.491
0.3	−1.379	+2.195	−1.493	+2.178	−1.501
0.8	−1.355	+2.194	−1.492	+2.176	−1.523
1.1	−1.335	+2.193	−1.490	+2.176	−1.544

number of surface substituted O atoms in (2×2) supercell QL Al_2S_3 monolayer, we study the connection between band offset, electrostatic potential difference, and surface charge redistribution.

C. Band offset with increased surface charge

The atomic configurations of substituted O atoms on tetrahedral termination surface from 1 to 3 are shown in Figs. 6(a)–6(c), respectively. When one to three O atoms are introduced into the supercell, the concentration of the doped O atom is 5% (at. %), 10% (at. %), and 15% (at. %) in QL Al_2S_3, respectively. Structurally, with increasing surface O atoms, the short Al-O bonds make the O-doped surface termination bulked. The corresponding band structures are depicted in Figs. 6(e)–6(g), respectively. With the surface O atom being from 1 to 2, the CBM and VBM move gradually to cross the E_F. The band gap decreases from 0.79 eV (indirect) to 0.21 eV (direct). When three O atoms are on the surface, the band gap disappears.

In order to clearly understand the band offset, the layer-resolved PDOSs of three configurations are shown in Figs. 6(h)–6(j). Since the PDOS of S(O) and Al atoms have nearly the same distribution [56], we only list the PDOS of four representive Al atoms [labeled in Fig. 6(a)]. Note that the CBM is contributed by Al4 atoms on surface tetrahedral termination in the three cases. From the atomic configuration, only the O-Al4 bond is increased synchronously with increasing surface O atoms. In addition, the conduction band from the Al2 atom also shifts down to E_F with increasing surface O atoms and O-Al2 bonds. With the number of the surface O atoms being from 1 to 3, the shifting CBM (n doping) and VBM (p doping) to the E_F means electrons are transferred to surface tetrahedral termination and holes are transferred to surface octahedral termination.

With the increasing surface O atoms, the $\Delta\phi$ enlarges gradually with the potential of Al_{tet} atoms becoming lower as shown in Figs. 6(k)–6(m). By changing the type of the group-VI element with different electronegativity, the electrostatic potential distribution also changes. The total $\Delta\phi$ in

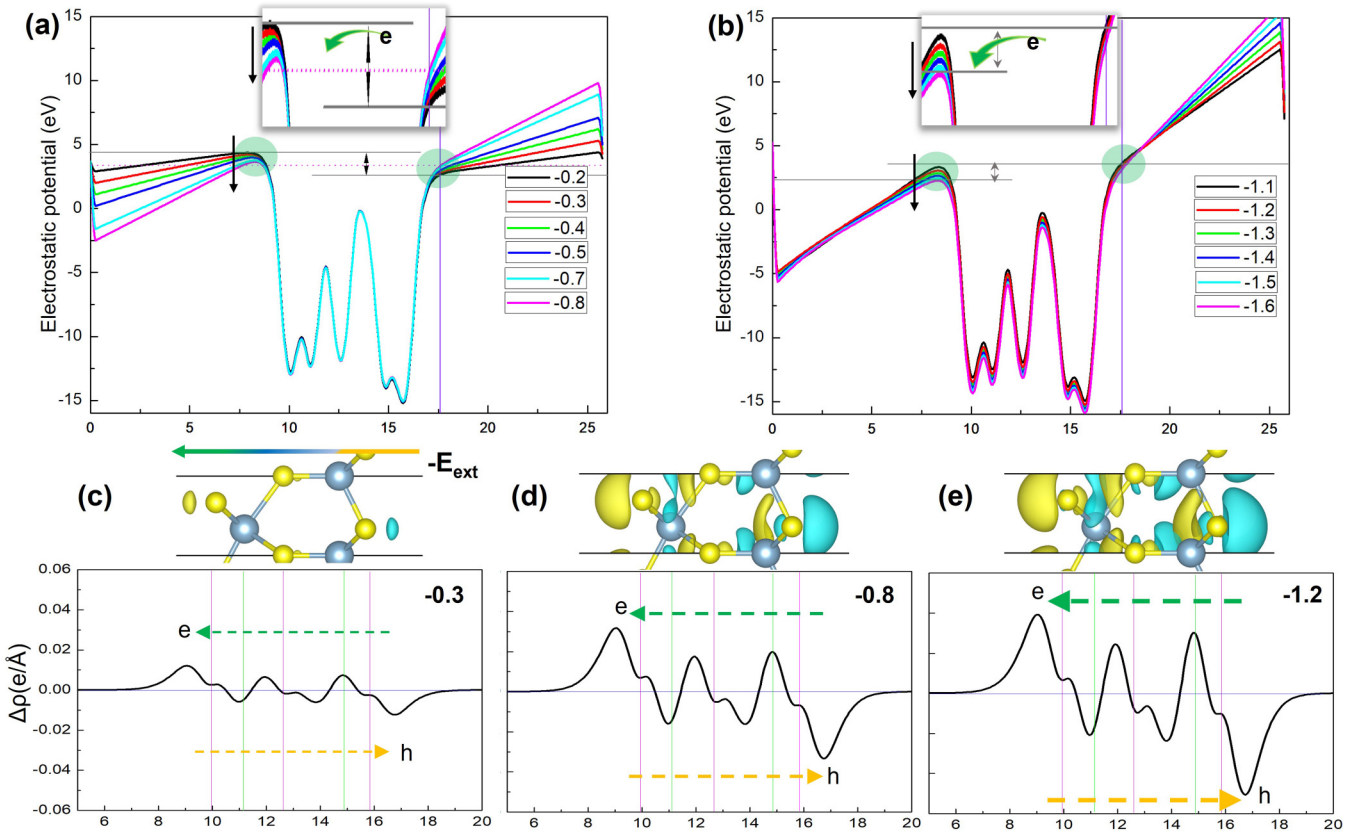

FIG. 9. (a), (b) The planar-averaged electrostatic potential distribution as a function of negative E_{ext} in QL Al_2S_3. (c)–(e) The charge density difference of QL Al_2S_3 under negative (−0.3, −0.8, −1.2 V/Å) electric field. The blue and yellow regions represent electron depletion and accumulation respectively.

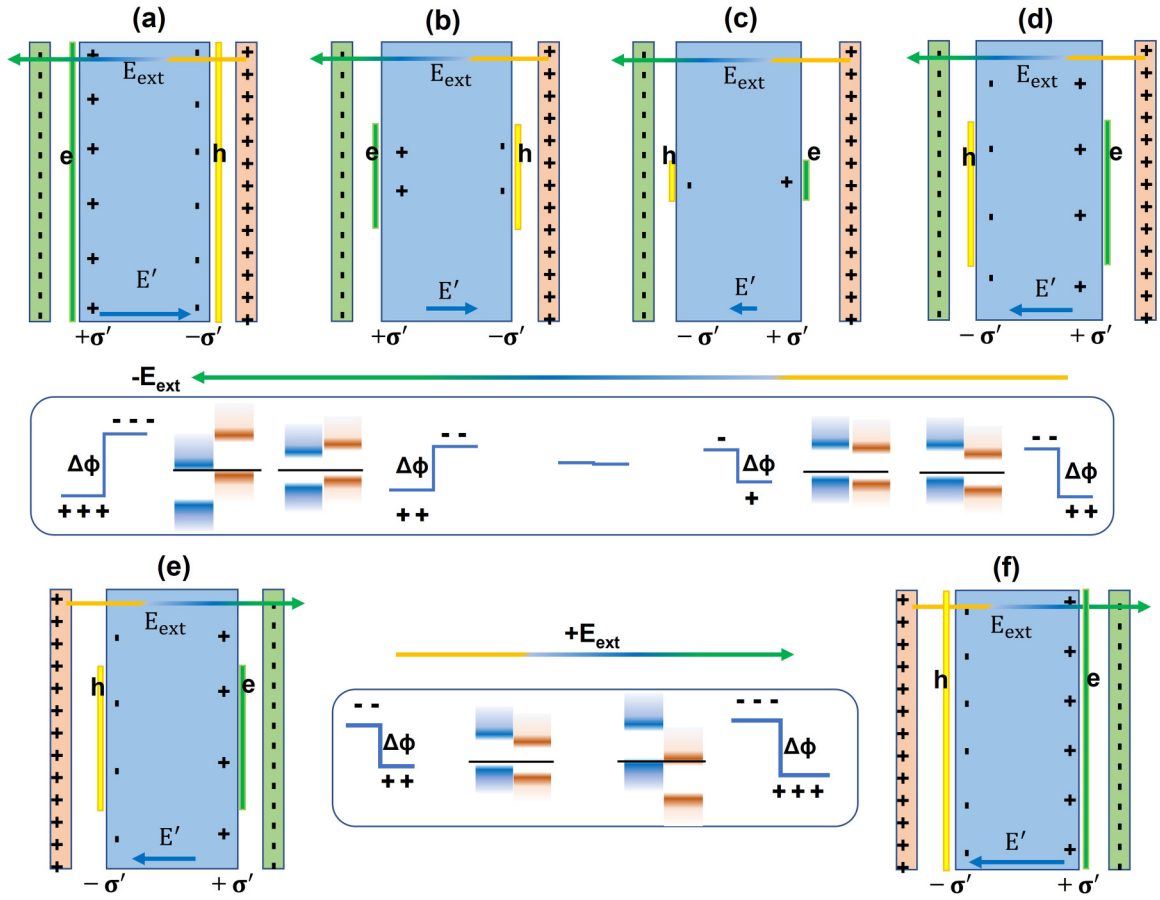

FIG. 10. Schematic diagram illustrates the separated bound charge (σ') distribution in QL Al_2S_3 under the negative (a)–(d) and positive (e), (f) E_{ext}. The schematic diagrams illustrate the synchronous change of $\Delta\phi$ and band offset from two surface atoms.

QL $Al_2S_2O_{tet}$ consists of two parts: One is from the structural asymmetry and another is from the electronegativity difference between S and O atoms. The increased $\Delta\phi$ reflects that more electrons are transferred from Al_{tet} atoms to the surface substituted O atom than the initial S atom (stronger electronegativity of the O atom than the S atom). It is worth noting that the total $\Delta\phi$ across QL Al_2S_3 increases gradually to a limit value [56,73,74].

Compared with QL Al_2S_3, QL $Al_2S_2O_{tet}$ turns into metal with enlarged $\Delta\phi$ and increased surface charge, while QL $Al_2S_2O_{oct}$ is still a semiconductor with the decreased $\Delta\phi$ and surface charge in Figs. 5(g) and 5(h). We also calculate the evolution of electric properties of QL Al_2S_3 with substituted O atoms on octahedral termination surface from 1 to 3; the band structures and PDOS show that they are still indirect band-gap semiconductors (see Fig. S3 in the Supplemental Material [68]). Our results fully show that the changed band offset and potential difference connect with the change of surface charge. More surface charge corresponds to the larger $\Delta\phi$ and smaller band gap in the Janus QL-$Al_2S_xO_{3-x}$ alloy phase.

D. Effect of external electric field on electronic properties

With the increasing intrinsic polarization electric field (or $\Delta\phi$) in QL Al_2S_3 by O doping, directional charge transfer is formed. As electron and hole move to two separate surfaces, *n*-type and *p*-type doping occur on the two surfaces of QL Al_2S_3, resulting in the semiconductor-metal transition in the system. The SMT mechanism induced by surface increased charge is verified through three evidences (shifting VBM and CBM, increased $\Delta\phi$, changed Bader charges) in the oxidized QL Al_2S_3 system. The premise for this SMT mechanism to work is the spatial separation of electron and hole. As we know, the separate surface charge (electron and hole) is one main characteristic in type-II heterostructure semiconductors. For type-II heterostructure semiconductors, previous research has reported its band structures may be easily changed by applying E_{ext} [43–51]. Next, by applying E_{ext} and directly changing the surface charge distribution on QL Al_2S_3, we investigate the evolution of band structures of QL Al_2S_3 and explain the connection between tunable band structures with surface charge distribution.

The band structures of QL Al_2S_3 with a series of different E_{ext} are shown in Figs. 7(a) and 7(b). The variable band gaps of QL Al_2S_3 as a function of E_{ext} are summarized in Figs. 7(c) and 7(d). When the E_{ext} points to the negative direction from 0 to -0.8 V/Å, the band gaps of QL Al_2S_3 increase gradually. When the E_{ext} continues to increase from -0.8 to -1.3 V/Å, the gaps decrease gradually to zero with the E_{ext} being above -1.3 V/Å. When the E_{ext} points to the positive direction from 0 to 0.8 V/Å, the gaps of QL Al_2S_3 decrease gradually to zero. When the E_{ext} continues to increase from 0.8 to 2.0 V/Å, the band gaps tend to be constant at zero. The tunable band

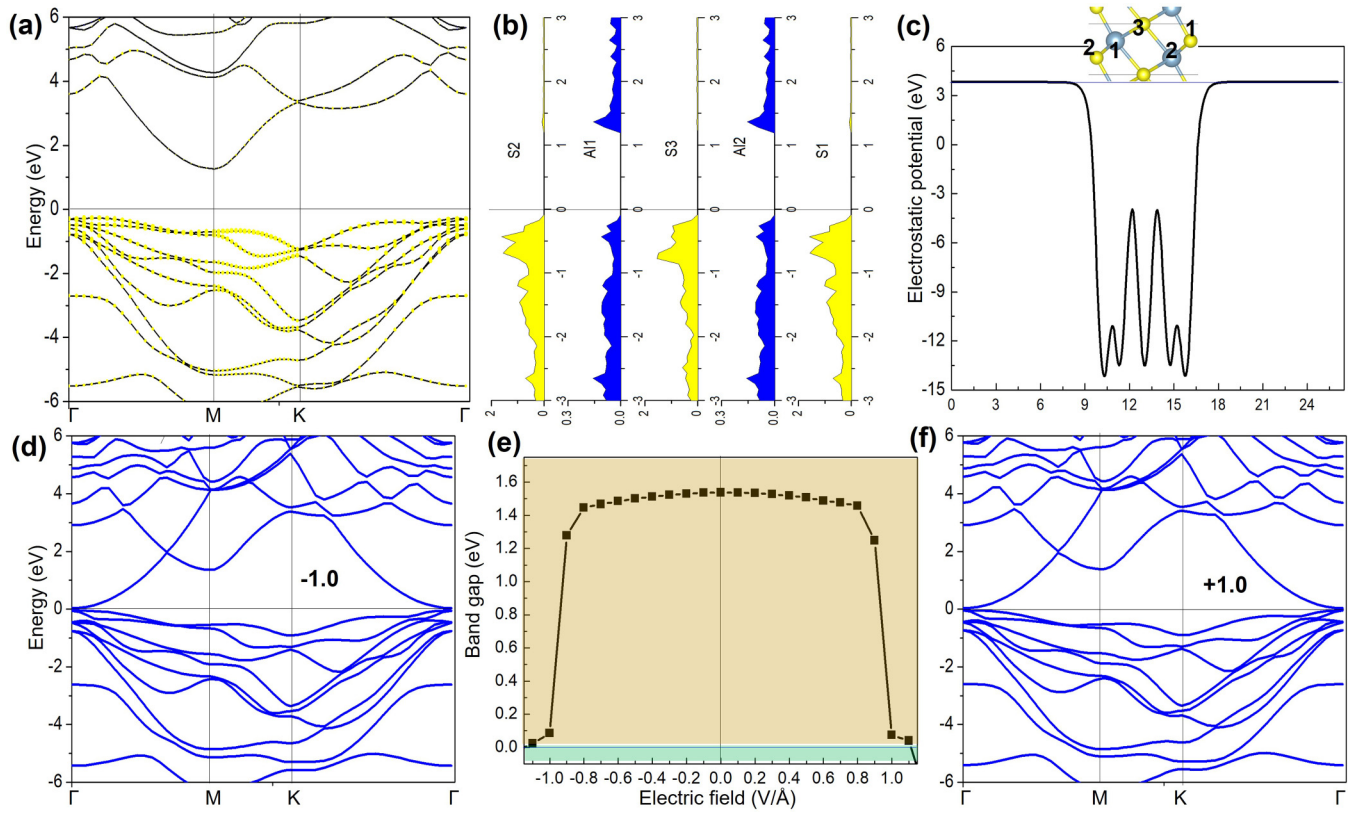

FIG. 11. (a), (b) The band structure and layer-resolved PDOS of S and Al atoms in PE Al_2S_3. All Fermi energy levels are shifted to zero. (c) The planar-averaged electrostatic potential of PE Al_2S_3 along the z axis. (d), (f) The band structure of PE Al_2S_3 under $-1.0\,V/Å$ and $+1.0\,V/Å$ electric field. (e) The band gap of PE Al_2S_3 as function of different external electric fields.

structures and SMT phenomenon of QL Al_2S_3 are surely present by applying E_{ext}.

From the above results, it is seen that the reduced band gap corresponds to the increased $\Delta\phi$, meaning that there is more surface charge in the oxidized QL-$Al_2S_2O_{tet}$ system. Does the change of band gap and $\Delta\phi$ still connect in QL Al_2S_3 by applying E_{ext}? The variable $\Delta\phi$ across QL Al_2S_3 under different E_{ext} is shown in Figs. 8(a) and 8(b). When the E_{ext} points to the positive direction from 0 to $1.0\,V/Å$, the potential of the Al_{tet} atom is gradually lower than the Al_{oct} atom termination, resulting in the larger $\Delta\phi$ across the QL Al_2S_3.

We have known that larger $\Delta\phi$ corresponds to the increased surface charge distribution and inner-layer charge transfer. To further clarify the transferred charge inside polarized monolayer, the planar-averaged charge density difference ($\Delta\rho$) is defined as $\Delta\rho = \rho * - \rho_0$, where ρ^* represents the charge density of QL Al_2S_3 under external electric field and ρ_0 represents the charge density of QL Al_2S_3 without electric field. Under the increasing positive direction E_{ext}, the amounts of transferred electron from the left Al_{oct} surface termination to the right Al_{tet} surface termination increase in Figs. 8(c)–8(e). The electron flow from high-potential (octahedral termination) to low-potential (tetrahedral termination) surface under the increasing E_{ext} is seen in Figs. 8(a) and 8(b) [56,71]. In addition, from the Bader charge analysis in Table III, we can clearly see the increased surface charge of the S atom on the tetrahedral termination and the decreased surface charge of the S atom on the octahedral termination under the increasing positive direction E_{ext}.

When the E_{ext} points to the negative direction from 0 to $-0.8\,V/Å$, the potential of the Al_{oct} atom is gradually lower than the Al_{tet} atom termination. The total $\Delta\phi$ across QL Al_2S_3 is gradually reduced to zero as shown in Fig. 9(a). This is also consistent with the previous calculation results [in Fig. 5(i)]. When the E_{ext} continues to increase from -1.1 to $-1.6\,V/Å$, the potential of the Al_{oct} atom is still gradually lower than the Al_{tet} atom termination, which results in the total $\Delta\phi$ across QL-Al_2S_3 increasing gradually in Fig. 9(b). From the planar-averaged charge density difference, it is clear that the amounts of transferred electron from the right Al_{tet} surface termination to the left Al_{oct} surface termination increase with increasing E_{ext} in Figs. 9(c)–9(e). From the Bader charge analysis in Table III, we can clearly see the increased surface charge of the S atom on octahedral termination and the decreased surface charge of the S atom on tetrahedral termination.

Actually, the QL Al_2S_3 under E_{ext} is similar to the dielectric in the parallel-plate capacitor in Fig. 10. Under the increasing positive direction E_{ext}, the surface bound and induced charge also increase. The increased surface charge (electron or hole) will drive the energy level (CBM or VBM) projected on two surface atoms to shift toward E_F. The increased surface charge is also reflected as the enlarged $\Delta\phi$,

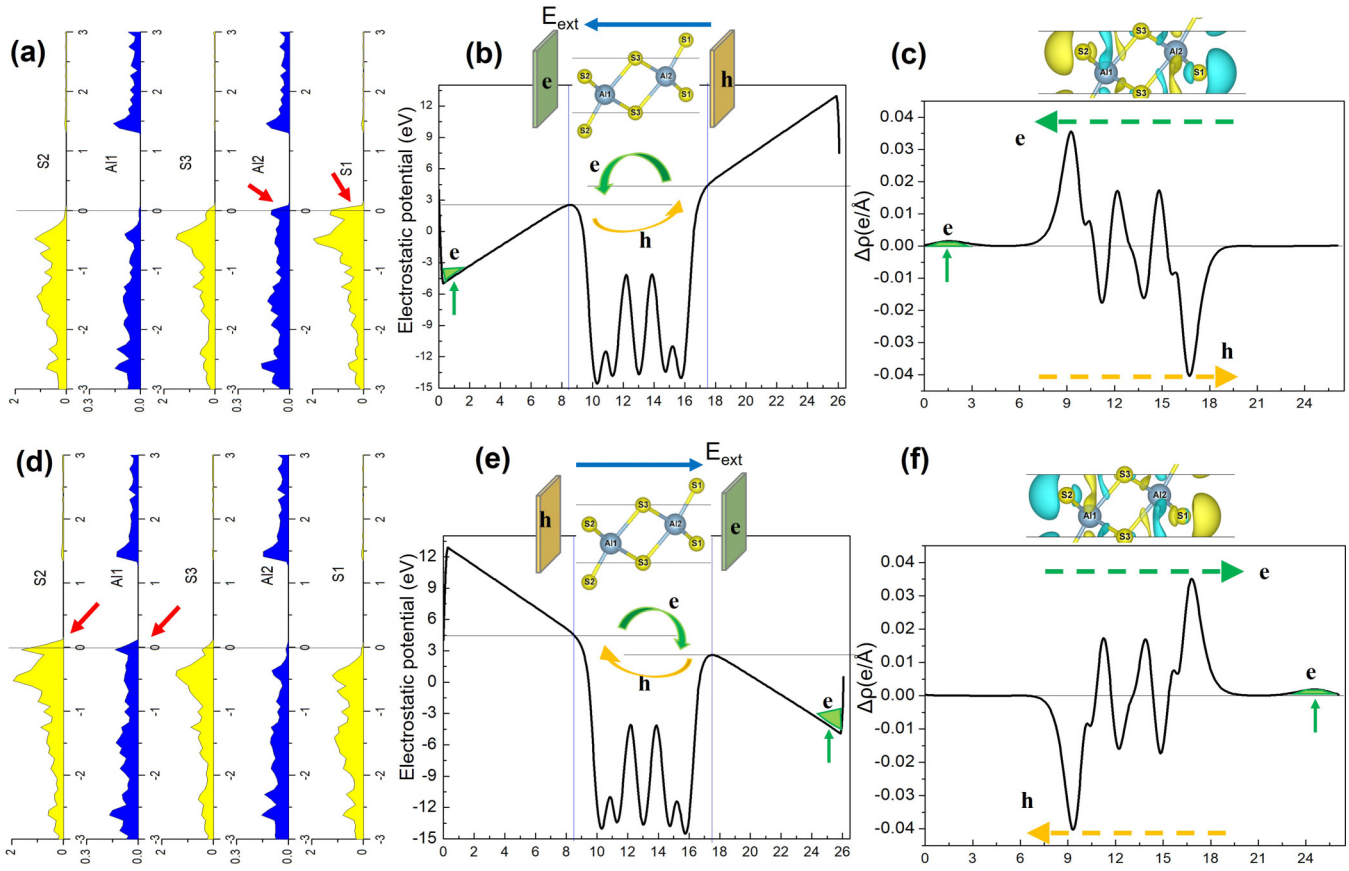

FIG. 12. (a) The layer-resolved PDOS of S and Al atoms and (b) the planar-averaged electrostatic potential of PE Al_2S_3 along the z axis under negative (-1.0 V/Å) electric field. (c) The charge density difference of PE Al_2S_3 along the z axis with and without negative (-1.0 V/Å) electric field. The blue and yellow region represents electron depletion and accumulation respectively. (d)–(f) The layer-resolved PDOS, planar-averaged electrostatic potential, charge density difference of PE Al_2S_3 under positive (1.0 V/Å) electric field.

since $\Delta\phi$ across the system reflect the strength of polarization electric field, which will drive charge transfer to the surface [56].

Under the increasing negative direction E_{ext}, first, the native surface (bound) charge decreases to zero. The reduced surface charge is also reflected as the reduced $\Delta\phi$ and increased band gap. Then, the new surface (bound) charge, opposite to the initial surface charge distribution (meaning polarization reversal), appears and increases with the increasing E_{ext}. With the increasing surface charge under the negative direction E_{ext}, the SMT also appears. The schematic diagram in Fig. 10 illustrates the changing surface (bound or induced) charge distribution with shifting CBM and VBM from two surface atoms and $\Delta\phi$ across monolayers under the E_{ext}.

IV. DISCUSSION

Two phenomena widely reported in previous research are summarized here: (1) The evolution of band offset, surface charge distribution (potential distribution), and inner-layer charge transfer are synergistic in 2D polar materials by tuning the polarization electric field or E_{ext} [71]. (2) The change of band gap in 2D polar materials under the increasing negative direction and positive direction E_{ext} are different [49–51]. For the first phenomenon, the increased surface charge distribution comes from the inner-layer charge transfer driven by increased electric field of polarization. In addition, the increased surface induced charge and polarization charge are consistent. For the second phenomenon, that is because of the existence of native surface polarization charge in QL Al_2S_3 with asymmetry structure. In other words, the native charge distribution of 2D monolayers plays an important role in determining the charge redistribution under E_{ext}.

For polar monolayers, the function of applying positive direction E_{ext} is equal to the increase of the native polarization electric field by oxidizing the tetrahedral termination in QL Al_2S_3. The function of applying negative direction E_{ext} is equal to decreasing the native polarization electric field (or increasing the opposite polarization electric field) by oxidizing the octahedral termination in QL Al_2S_3. The direction of electron motion is opposite to the direction of the polarization of the electric field, which means the driving force of electron motion is the increased polarization of the electric field. It is important to make sure that E_{ext} drive the motion of charge (electron, hole) through the monolayer.

For nonpolar monolayers, the native surface charge distribution is symmetric whether or not the surface charge shows different distribution by applying positive and negative direction E_{ext} in nonpolar monolayers. Next, taking the paraelectric phase Al_2S_3 monolayer (PE Al_2S_3) with symmetric structure

TABLE IV. Bader charges of PE-Al_2S_3 monolayer under negative and positive direction E_{ext}. Positive and negative values represent the electron depletion and accumulation.

E_{ext} (V/Å)	S	Al_{oct}	S	Al_{tet}	S
−1.0	−1.458	+2.190	−1.540	+2.190	−1.382
0.0	−1.420	+2.188	−1.539	+2.193	−1.422
1.0	−1.378	+2.183	−1.537	+2.192	−1.460

[in Fig. 2(d)] as example, we study the evolution of band offset, surface charge distribution (potential distribution), and inner-layer charge transfer by tuning the E_{ext}.

The band structure of PE-Al_2O_3 shows that it is an indirect band-gap semiconductor. The layer-resolved PDOS clearly shows that the CBM and VBM are equally distributed on the two separated surfaces of PE-Al_2S_3. The electrostatic potential of two surfaces termination is also the same, which means there is an even (nonpolar) charge distribution on the two surfaces of PE Al_2S_3. The variable band gaps of PE Al_2S_3 as a function of E_{ext} are summarized in Fig. 11(e). The change of band gap under positive and negative direction E_{ext} is nearly the same. The band structures of PE Al_2S_3 under negative and positive direction 1.0 V/Å electric field show the same shape, as shown in Figs. 11(d) and 11(f).

Although the band structure of PE Al_2S_3 under negative and positive direction 1.0−V/Å electric field is the same, the surface charge distribution is opposite, as shown in Figs. 12(a)–12(c) and 12(d)–12(f). Compared with the layer-resolved PDOS without E_{ext} in Fig. 11(b), the layer-resolved PDOS under the negative direction E_{ext} (−1.0 V/Å) clearly show that the VBM located at the right surface termination has passed the E_F in Fig. 12(a). The shifted VBM toward E_F represents the p doping and increased surface hole on the right surface of PE Al_2S_3. With the increase of negative direction E_{ext}, the potential of the left Al_{oct} atom is gradually lower than the right Al_{oct} atom termination; the larger $\Delta\phi$ across PE Al_2S_3 means more transferred charge through PE Al_2S_3, which behaves the same as in PE-Al_2S_3 in Fig. 9(b). The charge density difference clearly shows that the electron is depleted on the right surface and accumulated on the left surface, which means the electrons flow from the right PE Al_2S_3 surface (higher potential) to the left surface (lower potential). From the layer-resolved PDOS, the CBM does not pass through the E_F under E_{ext}. Actually, the accumulated electrons on the left surface of PE Al_2S_3 spill out under E_{ext}, as shown in Figs. 12(b) and 12(c) [75]. From the Bader charge analysis in Table IV, we can clearly see the increased surface charge of the S atom on the left termination and the decreased surface charge of the S atom on the right termination in PE Al_2S_3.

Compared with the layer-resolved PDOS without E_{ext} in Fig. 11(b), the layer-resolved PDOS of PE Al_2S_3 under the positive direction E_{ext} (1.0 V/Å) clearly shows the VBM located at the left surface in Fig. 12(d), which represents the p doping and increased surface hole. With the increase of positive direction E_{ext}, the potential of the right Al_{oct} atom is gradually lower than the left Al_{oct} atom termination, which behaves the same as in QL Al_2S_3 in Figs. 8(a) and 8(b). The larger $\Delta\phi$ across PE Al_2S_3 means more transferred charge through PE Al_2S_3. The charge density difference clearly shows that the electron is depleted on the left PE-Al_2S_3 surface and accumulates on the right PE-Al_2S_3 surface, which means the electrons flow from the higher potential to the lower potential. From the Bader charge analysis in Table IV, we can clearly see the increased surface charge of the S atom on the tetrahedral termination and the decreased surface charge of the S atom on the octahedral termination in PE Al_2S_3.

From the above results, we know that the SMT phenomenon in 2D polar or nonpolar monolayers under E_{ext} originates from the increased surface charge. There is one question here: Is the direction of transferred electron inside the monolayer parallel or antiparallel to the direction of the applied E_{ext}? The direction of transferred electron is the same as the direction of E_{ext} in QL Al_2S_3 and PE Al_2S_3, since the transferred electron inside the monolayer is induced by E_{ext}. The monolayer under E_{ext} is like a power source in the electric circuit in Figs. 12(a) and 12(b). Moreover, for polar monolayer, it is also similar to the *PN* junction being under forward bias or under illumination, as shown in Figs. 13(c)

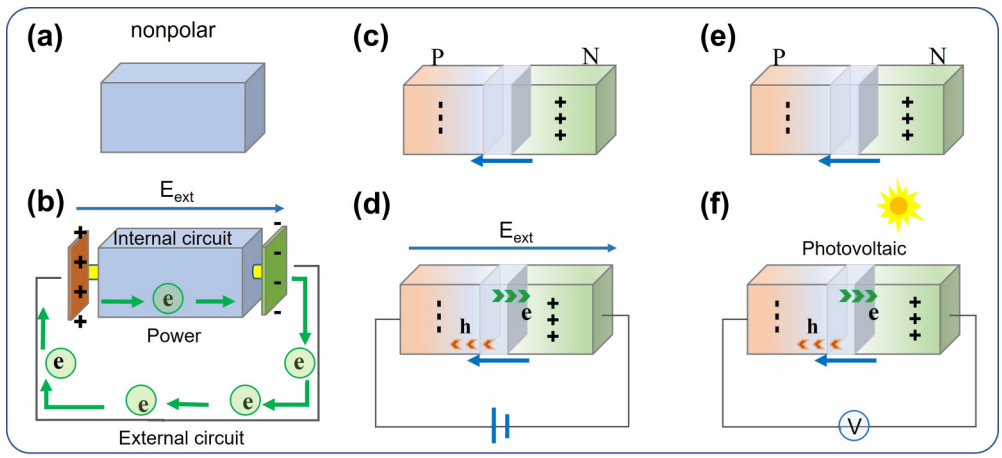

FIG. 13. (a), (b) The schematic diagram of inner-layer charge transfer inside nonpolar monolayer under external electric field. The schematic diagrams of spatially charged transfer of PN junction under forward bias (c), (d) and under illumination (e), (f).

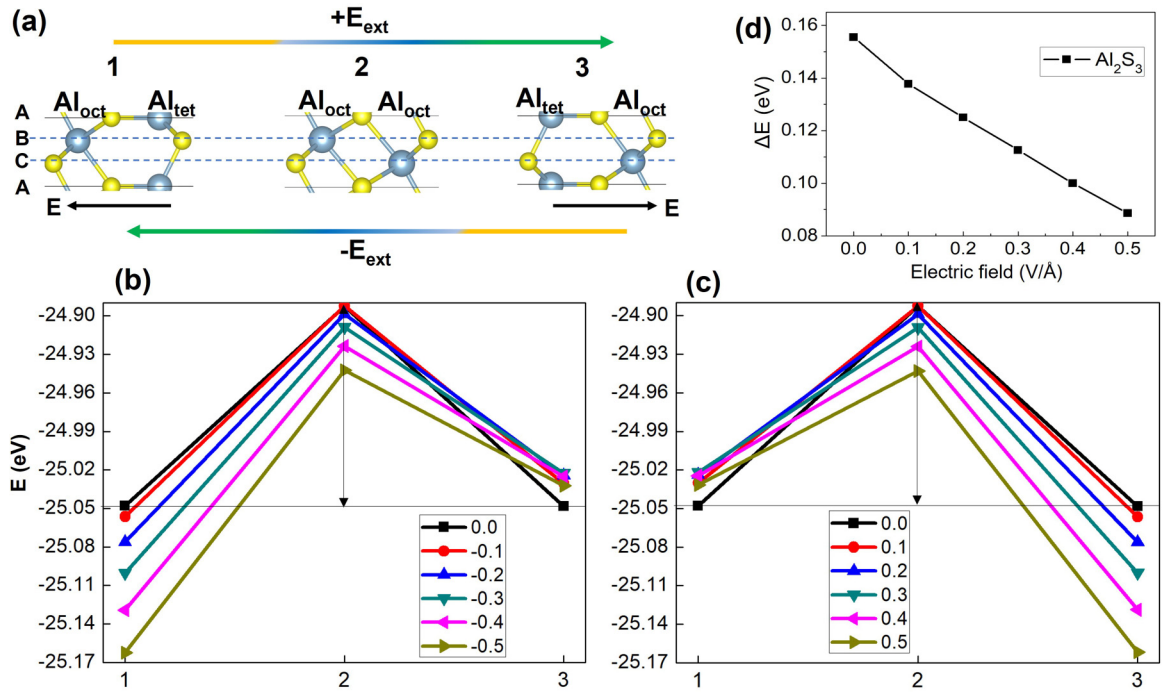

FIG. 14. (a) The two-step pathways of polarization reversal of QL Al_2S_3 with the O lattice atoms unmoving. (b), (c) The energy evolution of QL Al_2S_3 under negative and positive direction E_{ext} per unit cell. (d) The transition barrier of polarization reversal under positive direction E_{ext} per unit cell.

and 13(d) and 13(e) and 13(f). The essence of applying external electric field to a 2D system is applying extra potential difference through the system [76], which will redistribute the charge and drive the electron to flow from high potential to low potential.

We then investigated the effective kinetic pathway of the polarization reversal of QL Al_2S_3, as shown in Fig. 14: The initial state with the intrinsic polarization field E moves towards the left. The final state with the intrinsic polarization electric field E moves towards the right. The two-step pathways with the O lattice atoms are unmoving. First, the Al_{tet} (initial state) atom shifts from the A site to the C site. Second, the Al_{oct} (initial state) atom shifts from the B site to the A site.

The calculated polarization reversal barrier of QL Al_2S_3 is 0.155 eV per unit cell without E_{ext}. In order to illustrate the tunability of the reversal transition, the effect of the E_{ext} on the reduction of the transition barrier was studied. When the E_{ext} points to the negative direction from 0 to $-0.5\,V/Å$, the transition barrier is gradually increased as shown in Fig. 14(b). When the E_{ext} points to the positive direction from 0 to $0.5\,V/Å$, the transition barrier is gradually reduced in Fig. 14(c). The change of transition barrier under positive and negative direction E_{ext} are symmetric. Our results reveal that FE QL Al_2S_3 with operable polarization is an important and desired material for device applications.

V. CONCLUSIONS

In summary, we systematically investigate the semiconductor-to-metal transition in polarized QL Al_2S_3 by O substitution and applying external electric field. Our results have shown that both the band gap and electrostatic potential difference change with O-substituted and external electric field. The fundamental reason can be ascribed to the changed positive and negative surface charge at two sides in polarized QL Al_2S_3. The band alignment of type-II heterostructures means the interfacial charge transfer. The shifting band offset of polarized monolayers means the charge transfer inside the monolayer. The simple dielectric model clearly explains the connection between changing band structure and surface charge distribution, which is also applicable to other polarized 2D monolayer and heterostructure semiconductors.

ACKNOWLEDGMENT

This work was financially supported by the National Key Research and Development Program of China (Grants No. 2020YFA0406201 and No. 2021YFA1600701).

[1] J. Zhou, Q. Zeng, D. Lv, L. Sun, L. Niu, W. Fu, F. Liu, Z. Shen, C. Jin, and Z. Liu, Nano Lett. **15**, 6400 (2015).

[2] M. Küpers, P. M. Konze, A. Meledin, J. Mayer, U. Englert, M. Wuttig, and R. Dronskowski, Inorg. Chem. **57**, 11775 (2018).

[3] L. Liu, J. Dong, J. Huang, A. Nie, K. Zhai, J. Xiang, B. Wang, F. Wen, C. Mu, Z. Zhao *et al.*, Chem. Mater. **31**, 10143 (2019).

[4] J. Hou, S. Cao, Y. Sun, Y. Wu, F. Liang, Z. Lin, and L. Sun, Adv. Energy Mater. **8**, 1701114 (2018).

[5] Y. Zheng, X. Tang, W. Wang, L. Jin, and G. Li, Adv. Funct. Mater. **31**, 2008307 (2021).

[6] S. G. Parra, R. Vilaplana, O. Gomis, P. R. Hernández, A. Muñoz, J. A. González, J. A. Sans, C. Popescu, and F. J. Manjón, Chem. Mater. **34**, 6068 (2022).

[7] W. J. Ding, J. B. Zhu, Z. Wang, Y. F. Gao, D. Xiao, Y. Gu, Z. Y. Zhang, and W. G. Zhu, Nat. Commun. **8**, 14956 (2017).

[8] C.-F. Fu, J. Sun, Q. Luo, X. Li, W. Hu, and J. Yang, Nano Lett. **18**, 6312 (2018).

[9] E. F. Procopio, R. N. Pedrosa, F. A. L. de Souza, W. S. Paz, and W. L. Scopel, Phys. Chem. Chem. Phys. **22**, 3520 (2020).

[10] S. Baek, H. Yoo, J. H. Ju, P. Sriboriboon, P. Singh, J. Niu, J.-H. Park, C. Shin, Y. Kim, and S. Le, Adv. Sci. **9**, 2200566 (2022).

[11] M. Si, Z. Zhang, S.-C. Chang, N. Haratipour, D. Zheng, J. Li, U. Avci, and P. Ye, ACS Nano **15**, 5689 (2021).

[12] S. M. Poh, S. J. R. Tan, H. Wang, P. Song, I. H. Abidi, X. Zhao, J. Dan, J. Chen, Z. Luo, S. J. Pennycook, A. Neto, and K. P. Loh, Nano Lett. **18**, 6340 (2018).

[13] S. Wan, Y. Li, W. Li, X. Mao, C. Wang, C. Chen, J. Dong, A. Nie, J. Xiang, Z. Liu *et al.*, Adv. Funct. Mater. **29**, 1808606 (2019).

[14] Z. Wang, X. Liu, X. Zhou, Y. Yuan, K. Zhou, D. Zhang, H. Luo, and J. Sun, Adv. Mater. **34**, 2200032 (2022).

[15] Z. J. Wang and Y. Bai, Small **15**, 1805088 (2019).

[16] H. J. Jin, C. Park, K. J. Lee, G. H. Shin, and S.-Y. Choi, Adv. Mater. Technol. **6**, 2100494 (2021).

[17] Y. Zhao, F. Guo, R. Ding, F. I. Weng, S.-Y. Pang, W. Wu, and J. Hao, Adv. Opt. Mater. **9**, 2100864 (2021).

[18] G. Almeida, S. Dogan, G. Bertoni, C. Giannini, R. Gaspari, S. Perissinotto, R. Krahne, S. Ghosh, and L. Manna, J. Am. Chem. Soc. **139**, 3005 (2017).

[19] Y. Zhou, D. Wu, Y. Zhu, Y. Cho, Q. He, X. Yang, K. Herrera, Z. Chu, Y. Han, M. C. Downer *et al.*, Nano Lett. **17**, 5508 (2017).

[20] J. H. Dycus, K. J. Mirrielees, E. D. Grimley, R. Kirste, S. Mita, Z. Sitar, R. Collazo, D. L. Irving, and J. M. LeBeau, ACS Appl. Mater. Interfaces **10**, 10607 (2018).

[21] B. Meng, T. Jing, and W.-Z. Xiao, Comput. Mater. Sci. **200**, 110775 (2021).

[22] X. Jin, Y.-Y. Zhang, S. T. Pantelides, and S. Du, Nanoscale Horiz. **5**, 1303 (2020).

[23] T. V. Vu and N. N. Hieu, J. Phys.: Condens. Matter **34**, 115601 (2022).

[24] Y.-W. Son, M. L. Cohen, and S. G. Louie, Nature (London) **444**, 347 (2006).

[25] E.-J. Kan, Z. Li, J. Yang, and J. G. Hou, Appl. Phys. Lett. **91**, 243116 (2007).

[26] S. Thiel, G. Hammerl, A. Schmehl, C. W. Schneider, and J. Mannhart, Science **313**, 1942 (2006).

[27] H. Lee, N. Campbell, J. Lee, T. J. Asel, T. R. Paudel, H. Zhou, J. W. Lee, B. Noesges, J. Seo, B. Park *et al.*, Nat. Mater. **17**, 231 (2018).

[28] C. H. Ahn, J.-M. Triscone, and J. Mannhart, Nature (London) **424**, 1015 (2003).

[29] R. Meng, M. Houssa, K. Iordanidou, G. Pourtois, V. Afanasiev, and A. Stesmans, Phys. Rev. Mater. **4**, 074001 (2020).

[30] M.-Y. Liu, Y. He, Y. Mao, and K. Xiong, Phys. Rev. B **105**, 035418 (2022).

[31] X. Li, Xi Zuo, H. Li, L. Han, Q. Gao, D. Li, B. Cui, D. Liu, and F. Qu, Phys. Chem. Chem. Phys. **21**, 19234 (2019).

[32] H. Ai, F. Li, H. Bai, D. Liu, K. H. Lo, S. A. Yang, Y. Kawazoe, and H. Pan, npj Comput. Mater. **8**, 60 (2022).

[33] Y. Liao, Z. Zhang, Z. Gao, Q. Qian, and M. Hua, ACS Appl. Mater. Interfaces **12**, 30659 (2020).

[34] N. N. Hieu, H. V. Phuc, A. I. Kartamyshev, and T. V. Vu, Phys. Rev. B **105**, 075402 (2022).

[35] R. Xiong, W. Li, Y. Zhang, Z. Cui, C. Wen, M. Anpo, B. Wu, and B. Sa, J. Mater. Chem. C **10**, 10480 (2022).

[36] S. Demirci, N. Avazlı, E. Durgun, and S. Cahangirov, Phys. Rev. B **95**, 115409 (2017).

[37] T. V. Vu, C. V. Nguyen, H. V. Phuc, A. A. Lavrentyev, O. Y. Khyzhun, N. V. Hieu, M. M. Obeid, D. P. Rai, H. D. Tong, and N. N. Hieu, Phys. Rev. B **103**, 085422 (2021).

[38] M. Demirtas, B. Ozdemir, Y. Mogulkoc, and E. Durgun, Phys. Rev. B **101**, 075423 (2020).

[39] M. Demirtas, M. J. Varjovi, M. M. Cicek, and E. Durgun, Phys. Rev. Mater. **4**, 114003 (2020).

[40] T. V. Vu, T. P. T. Linh, H. V. Phuc, C. A. Duque, A. I. Kartamyshev, and N. N. Hieu, J. Phys.: Condens. Matter **34**, 045501 (2022).

[41] T. V. Vu, V. T. T. Vi, H. V. Phuc, A. I. Kartamyshev, and N. N. Hieu, Phys. Rev. B **104**, 115410 (2021).

[42] L. Debbichi, O. Eriksson, and S. Lebègue, J. Phys. Chem. Lett. **6**, 3098 (2015).

[43] L. Xu, W.-Q. Huang, W. Hu, K. Yang, B.-X. Zhou, A. Pan, and G.-F. Huang, Chem. Mater. **29**, 5504 (2017).

[44] D. Chen, X. Lei, Y. Wang, S. Zhong, G. Liu, B. Xu, and C. Ouyang, Appl. Surf. Sci. **497**, 143809 (2019).

[45] Z. Xie, F. Sun, R. Yao, Y. Zhang, Y. Zhang, Z. Zhang, J. Fan, L. Ni, and L. Duan, Appl. Surf. Sci. **475**, 839 (2019).

[46] R. Zhang, Y. Zhang, X. Wei, T. Guo, J. Fan, L. Ni, Y. Weng, Z. Zha, J. Liu, Y. Tian *et al.*, Appl. Surf. Sci. **528**, 146782 (2020).

[47] X. Li, B. Zhai, X. Song, Y. Yan, J. Li, and C. Xia, Appl. Surf. Sci. **509**, 145317 (2020).

[48] X. Li, G. Jia, J. Du, X. Song, C. Xia, Z. Wei, and J. Li, J. Mater. Chem. C **6**, 10010 (2018).

[49] L. Huang, N. Huo, Y. Li, H. Chen, J. Yang, Z. Wei, J. Li, and S.-S. Li, J. Phys. Chem. Lett. **6**, 2483 (2015).

[50] W. Li, T. Wang, X. Dai, Y. Ma, and Y. Tang, J. Alloy. Compd. **705**, 486(2017).

[51] B. Zhou, K. Jiang, L. Shang, J. Zhang, Y. Li, L. Zhu, S.-J. Gong, Z. Hu, and J. Chu, J. Mater. Chem. C **8**, 11160 (2020).

[52] M. Wang, S. Cai, C. Pan, C. Wang, X. Lian, Y. Zhuo, K. Xu, T. Cao, X. Pan, B. Wang *et al.*, Nat. Electron. **1**, 130 (2018).

[53] Q. Chen, M. Chen, L. Zhu, N. Miao, J. Zhou, G. J. Ackland, and Z. Sun, ACS Appl. Mater. Interfaces **12**, 45184 (2020).

[54] D. Xiao, D.-L. Bao, X. Liang, Y. Wang, J. Shen, C. Cheng, and P. K. Chu, Appl. Catal. B: Environ. **288**, 119983 (2021).

[55] Z. Fang, E. H. Wang, Y. F. Chen, X. M. Hou, K.-C. Chou, W. Y. Yang, J. H. Chen, and M. H. Shang, ACS Appl. Mater. Interfaces **10**, 30811 (2018).

[56] X. Wang, J. Xu, J. Si, B. Wang, and W. Yin, Appl. Surf. Sci. **610**, 155614 (2023).

[57] G. Kresse and J. Furthmuller, Phys. Rev. B **54**, 11169 (1996).

[58] W. Kohn and L. J. Sham, Phys. Rev. **140**, A1133 (1965).

[59] P. E. Blöchl, Phys. Rev. B **50**, 17953 (1994).

[60] J. P. Perdew, K. Burke, and M. Ernzerhof, Phys. Rev. Lett. **77**, 3865 (1996).

[61] J. Heyd, G. E. Scuseria, and M. Ernzerhof, J. Chem. Phys. **118**, 8207 (2003).
[62] G. Henkelman, A. Arnaldsson, and H. Jónsson, Comput. Mater. Sci. **36**, 354 (2006).
[63] T. Sohier, M. Calandra, and F. Mauri, Phys. Rev. B **96**, 075448 (2017).
[64] S. Nosé, J. Chem. Phys. **81**, 511 (1984).
[65] S. Baroni, S. de Gironcoli, A. Dal Corso, and P. Giannozzi, Rev. Mod. Phys. **73**, 515 (2001).
[66] V. Wang, N. Xu, J.-C. Liu, G. Tang, and W.-T. Geng, Comput. Phys. Commun. **267**, 108033 (2021).
[67] K. Momma and F. Izumi, J. Appl. Cryst. **44**, 1272 (2011).
[68] See Supplemental Material at http://link.aps.org/supplemental/10.1103/PhysRevB.107.235307 for phonon spectra, PHDOS, and relaxed atomic configurations in the process of AIMD calculations of QL-$Al_2S_2O_{tet}$ and QL-$Al_2S_2O_{oct}$ monolayer, and the evolution of electronic band structures and layer-resolved PDOS of (2×2) supercell QL Al_2S_3 with increased surface O atoms on octahedral termination.
[69] M. A. Khan, M. A. Nadeem, and H. Idriss, Surf. Sci. Rep. **71**, 1 (2016).
[70] W. Dong, H. Xiao, Y. Jia, L. Chen, H. Geng, S. U. H. Bakhtiar, Q. Fu, and Y. Guo, Adv. Sci. **9**, 2105368 (2022).
[71] X. Wang, J. Xu, P.-F. Liu, B.-T. Wang, and W. Yin, J. Mater. Chem. A **11**, 10628 (2023).
[72] C. Zhu, J. Yang, P. Shan, M.-H. Zhao, S. Zhao, C. Pei, B. Zhang, Z. Deng, M. Croft, Y. Qi *et al.*, CCS Chem. **5**, 934 (2022).
[73] M. Soleimani and M. Pourfath, Nanoscale **12**, 22688 (2020).
[74] R. Peng, Y. D. Ma, S. Zhang, B. B. Huang, L. Z. Kou, and Y. Dai, Mater. Horiz. **7**, 504 (2020).
[75] X.-P. Wang, X.-B. Li, N.-K. Chen, J.-H. Zhao, Q.-D. Chen, and H.-B. Sun, Phys. Chem. Chem. Phys. **20**, 6945 (2018).
[76] H. Wang, J. Bang, Y. Sun, L. Liang, D. West, V. Meunier, and S. Zhang, Nat. Commun. **7**, 11504 (2016).